AIAA JOURNAL
Vol. 34, No. 4, April 1996

Numerical Simulation of Transient Hypersonic Flow Using the Essentially Nonoscillatory Schemes

Chien-Erh Chiu* and Xiaolin Zhong†
University of California, Los Angeles, Los Angeles, California 90095

Numerical simulation of transient hypersonic flows involving shock-wave–freestream-disturbance interactions is presented using the essentially nonoscillatory (ENO) schemes. The ENO schemes were chosen for transient-flow simulations because they have high-order accuracy at extrema as well as in other parts of smooth solutions. First, the accuracy of the ENO schemes was tested numerically by applying them to the computations of a one-dimensional linear model equation and to an oscillating plate problem using the two-dimensional Navier–Stokes equations. Then, the third-order ENO scheme was used to compute the unsteady interaction of a freestream acoustic wave with a bow shock in hypersonic flow past a cylinder. The numerical results along the stagnation line were compared with linearized analytical solutions. The results show that the disturbance waves generated behind the bow shock are significantly amplified by the back-and-forth interactions and reflections of the acoustic waves. These results on the bow-shock–disturbance interactions will be useful in understanding the effects of the bow shock wave on the receptivity of hypersonic boundary layers to freestream disturbances.

Nomenclature

A_{p+}, etc.	= disturbance-wave amplitude
c	= speed of sound behind the shock
c_p	= specific heat at constant pressure
c_1	= speed of sound ahead of the shock
d	= distance between the shock and the body
e	= total energy per unit volume
$\boldsymbol{F}_e, \boldsymbol{F}_v, \boldsymbol{G}_e, \boldsymbol{G}_v$	= flux vectors
M	= Mach number behind the shock
M_1	= Mach number ahead of the shock
p	= pressure behind the shock
p_+, p_-, etc.	= perturbation variables
p_1	= pressure ahead of the shock
q_i	= components of the heat-flux vector
s	= entropy
T	= temperature
t	= time
$\boldsymbol{U}$	= vector of flow variables
u, u_{ij}, v	= velocity components
W	= vorticity
x, y, x_i	= Cartesian coordinates
γ	= ratio of specific heats
δp, etc.	= wave perturbation variables
κ	= coefficient of thermal conductivity
μ	= viscosity coefficient
Π_{ij}, Λ_{ij}	= coefficients in linearized shock relations
ρ	= density
σ_{ij}	= viscous stress tensor
ψ	= perturbed shock displacement
ω	= wave frequency

Subscripts

∞	= freestream variables
$+$	= variables behind the shock
$-$	= variables ahead of the shock

Presented as Paper 95-0469 at the AIAA 33rd Aerospace Sciences Meeting, Reno, NV, Jan. 9–12, 1995; received March 20, 1995; revision received Oct. 6, 1995; accepted for publication Nov. 3, 1995.

*Graduate Student, Mechanical, Aerospace and Nuclear Engineering Department. Member AIAA.

†Assistant Professor, Mechanical, Aerospace and Nuclear Engineering Department. Member AIAA.

Introduction

RESEARCH on hypersonic flows has focused mainly on developing real-gas models and computing steady hypersonic flows, but the unsteadiness of hypersonic flows has not received serious attention. There are many practical problems where flowfield unsteadiness or instability can have strong effects on aerodynamic loads and heating rates to hypersonic vehicles.[1] Examples of such unsteady flows include flows around maneuvering hypersonic vehicles, the instability and transition of hypersonic boundary layers,[2] unstable shock-on-shock interference heating in a hypersonic inlet,[3] and the interactions of bow shock waves with freesteam disturbances in hypersonic flows past blunt leading edges.[4] This paper deals with numerical simulation of such transient hypersonic flows. In particular, preliminary studies were conducted on the unsteady bow-shock–disturbance interaction problem using numerical simulations.

The bow-shock–disturbance interaction problem originates from studies of the receptivity of hypersonic boundary layers to freestream disturbances. The receptivity, which refers to the processes by which the environmental disturbances initially enter the boundary layers and generate linear instability waves,[5] is an important aspect of transition from laminar to turbulent states of boundary layers. For hypersonic flow past a blunt leading edge, the bow shock wave has strong effects on the stability and transition of the boundary layer behind the shock. The curved bow shock creates entropy and vorticity layers, which are eventually swallowed by the boundary layer. In addition, the unsteady interaction of a freestream disturbance wave with the bow shock produces three kinds of disturbance waves: acoustic, entropy, and vorticity waves. These waves propagate independently toward the solid surface where the acoustic wave is reflected from the wall. The reflected acoustic wave then propagates upstream and changes the waves behind the shock when it interacts with the shock from behind. These back-and-forth wave reflections and interactions cause considerable changes in all three disturbance waves behind the shock and raise the question of whether the bow shock wave is stable in such interactions.

Morkovin[4] assessed the bow-shock–disturbance interaction along the stagnation line using a one-dimensional linear analytical model. A general knowledge of the interaction process was obtained by this approximate analysis. However, this one-dimensional linear model can be applied only to the stagnation line with the assumption of uniform flow behind the shock where the actual flow is nonuniform. Furthermore, the model does not explain how the vorticity field is affected by the wave interactions and reflections. Numerical simulations are needed to study the complete two-dimensional flow properties of the bow-shock–disturbance wave interactions.

The simulations for such flows are difficult to accomplish because they not only need to capture the shock waves without spurious numerical oscillations but also need to resolve small-magnitude physical fluctuations of the disturbance waves. The disturbance-wave computations require numerical methods with high-order accruacy, but the shock-capturing computations need to reduce to first-order accuracy at the shock to avoid numerical oscillations. As a result, an appropriate numerical method needs to have locally high-order accuracy in the smooth regions of the flowfields and to be nonoscillatory across shock waves.

Among current high-resolution shock-capturing schemes, the essentially nonoscillatory (ENO) schemes[6] are chosen for such computations because they have formally high-order accuracy in smooth regions of the flowfields and are nonoscillatory across shock waves. Though the total variation diminishing (TVD) schemes have been the most popular methods for hypersonic flow computations, they reduce to first-order accuracy at local extrema of solutions. As a result, the TVD schemes are most suitable for steady and moderately unsteady flow computations where the physical solutions do not contain many extrema, but they can be very numerically diffusive for computing oscillatory wave solutions. The ENO schemes were developed to improve the accuracy of the TVD schemes at the local extrema of smooth solutions. But the main drawback of the ENO schemes is that they are less stable for steady-flow computations because the TVD condition is not strictly satisfied in the ENO schemes. Many modifications have been proposed to reduce the oscillations of the ENO schemes.[7–9]

We continued to apply the ENO schemes to transient hypersonic flow computations.[3] First, we quantitatively tested the numerical accuracy of the ENO schemes for solving model problems relevant to transient viscous flow simulations using a convection–diffusion equation and the two-dimensional Navier–Stokes equations. We did not attempt to conduct exhaustive tests to validate the accuracy of the ENO schemes; other test results for ENO schemes can be found in Refs. 3 and 10–15. Second, we computed a freestream acoustic wave interacting with the bow shock in front of a cylinder moving at a hypersonic speed. Inviscid flow in a perfect gas was assumed to focus the attention on the effects of bow-shock–disturbance wave interactions outside the boundary layer.

Governing Equations

The Navier–Stokes equations written in the conservation-law form in Cartesian coordinates are

$$\frac{\partial \boldsymbol{U}}{\partial t}+\frac{\partial \boldsymbol{F}_e}{\partial x}+\frac{\partial \boldsymbol{F}_v}{\partial x}+\frac{\partial \boldsymbol{G}_e}{\partial y}+\frac{\partial \boldsymbol{G}_v}{\partial y}=0 \tag{1}$$

where $\boldsymbol{U}=[\rho, \rho u, \rho v, e]^T$ and

$$\boldsymbol{F}_e=\begin{bmatrix}\rho u\\ \rho u^2+p\\ \rho uv\\ (e+p)u\end{bmatrix},\qquad \boldsymbol{F}_v=\begin{bmatrix}0\\ \sigma_{11}\\ \sigma_{12}\\ \sigma_{11}u+\sigma_{12}v+q_1\end{bmatrix}$$

$$\boldsymbol{G}_e=\begin{bmatrix}\rho v\\ \rho uv\\ \rho v^2+p\\ (e+p)v\end{bmatrix},\qquad \boldsymbol{G}_v=\begin{bmatrix}0\\ \sigma_{21}\\ \sigma_{22}\\ \sigma_{21}u+\sigma_{22}v+q_2\end{bmatrix} \tag{2}$$

$$e=[p/(\gamma-1)]+(\rho/2)(u^2+v^2) \tag{3}$$

The viscous-stress and heat-flux terms are given by

$$\sigma_{ij}=-\mu\left(\frac{\partial u_i}{\partial x_j}+\frac{\partial u_j}{\partial x_i}-\frac{2}{3}\delta_{ij}\frac{\partial u_k}{\partial x_k}\right),\qquad q_i=-\kappa\frac{\partial T}{\partial x_i} \tag{4}$$

where the viscosity coefficient μ is computed according to Sutherland's law; and the heat conductivity κ is determined by assuming a constant Prandtl number.

Numerical Methods

Both the Euler and the Navier–Stokes equations are solved by the ENO schemes using finite volume formulations.[6,12] At computational cell boundaries, the inviscid flux terms are computed by the high-order two-dimensional ENO reconstruction proposed by Casper[12]; the viscous-flux terms are computed by second- or forth-order-accurate fixed-stencil central difference schemes. The equations are advanced in time using the explicit TVD Runge–Kutta schemes derived by Shu and Osher.[10] Details of the numerical methods can be found in Ref. 16.

Numerical Tests of the ENO Schemes

Linear Convection–Diffusion Equation

The following one-dimensional model equation was used to test the accuracy of the ENO schemes:

$$\frac{\partial u}{\partial t}+c\frac{\partial u}{\partial x}=\mu\frac{\partial^2 u}{\partial x^2} \tag{5}$$

where $c=1$, $\mu=5\times10^{-3}$, and $u(x,t=0)=\sin^4\pi x$. Equation (5) was solved in the computational domain of $-1\le x\le 1$ using the ENO schemes of various accuracies ranging from the first to the sixth order. The computations were advanced in time in one period using a Courant–Friedrichs–Lewy (CFL) number of 0.1 based on $\mathrm{CFL}=c\Delta t/\Delta x$.

Figure 1 shows numerical errors measured by the L_1 norm vs the numbers of grid points. The original ENO schemes and the ENO schemes with modification introduced by Shu[8] maintain their theoretical accuracy in computing Eq. (5). In Fig. 2, the numerical solutions of 40 grid points obtained by using the ENO schemes are compared with the exact solution. Since the numerical results of second-order accuracy introduce significant damping to the wave solutions, it is necessary to use high-order schemes for wave computations.

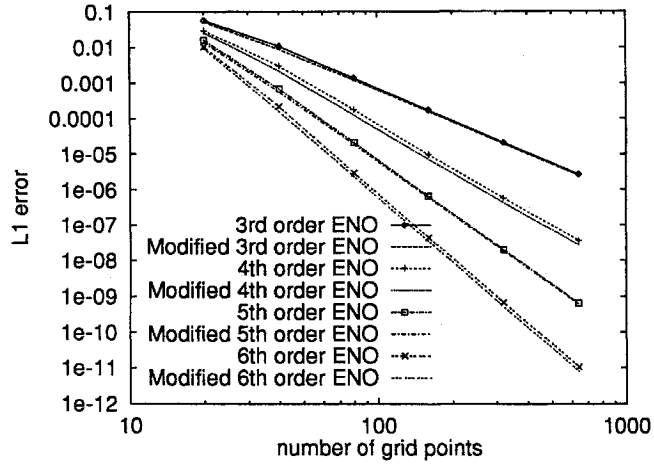

Fig. 1 Grid refinement study for convection–diffusion equation with $u(x,0)=\sin^4 x$.

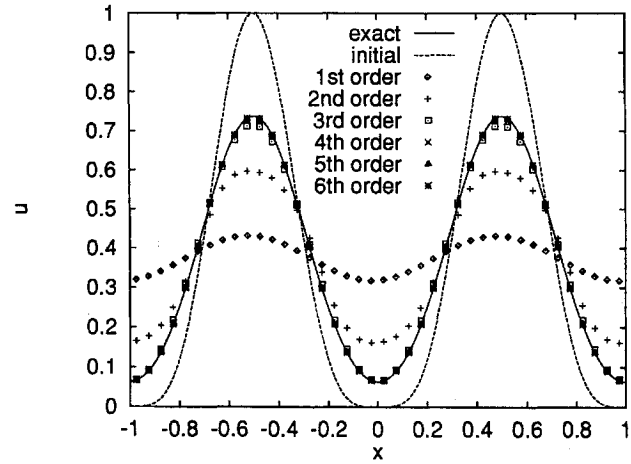

Fig. 2 Numerical solutions of convection–diffusion equation obtained by the ENO schemes with $u(x,0)=\sin^4 x$.

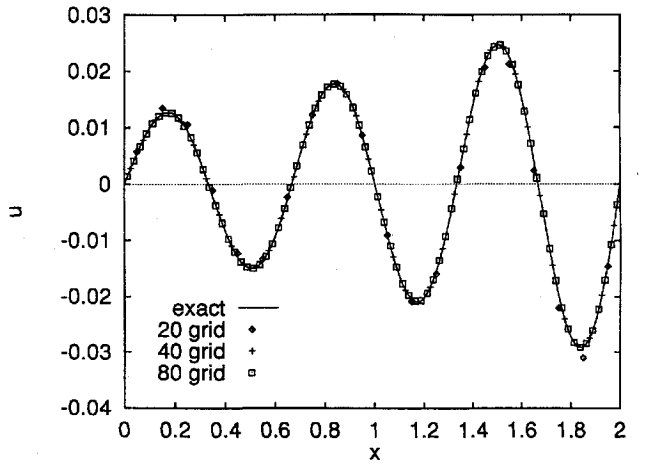

Fig. 3 Numerical solutions of convection–diffusion equation obtained by the ENO schemes with $u(x, 0) = e^{0.5x} \sin 3\pi x$.

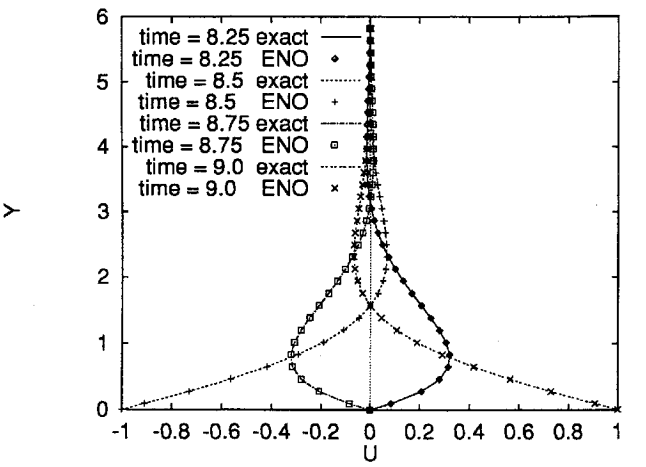

Fig. 4 Instantaneous solutions of Stokes oscillating plate at various cycles.

Next, the effect of boundary conditions on the accuracy of the ENO schemes was tested by computing Eq. (5) with the following boundary conditions:

$$u(0, t) = u(l, t) = 0 \tag{6}$$

The general solutions of this boundary-value problem are

$$u(x, t) = \sum_{n=1}^{\infty} A_n \exp(k_n t)\phi_n(x) \tag{7}$$

where A_n is determined by initial conditions, and the eigenvalues and eigenfunctions are

$$\begin{aligned} k_n &= -(1/4\mu)[(n\pi\mu/l)^2 + c^2] \\ \phi_n(x) &= \exp[(c/2\mu)x] \sin(n\pi/l)x \end{aligned} \tag{8}$$

The modified fourth-order ENO scheme was used to solve the initial-boundary-value problem with $c = 1$, $\mu = 1$, $l = 2$, and an initial condition of $u(x, t = 0) = \phi_m(x)$. The exact solution is

$$u(x, t) = \exp(k_m t)\phi_m(x) \tag{9}$$

The numerical solutions were obtained at $t = 0.05$ with CFL number based on inviscid variables to be 0.001 (CFL $= c\Delta t/\Delta x$). Again, grid refinement studies show that numerical results maintain the theoretical accuracy of the ENO schemes.[16] Figure 3 compares the numerical and exact solutions. The modified ENO schemes performed well in computations for this initial-boundary-value problem.

Stokes Oscillating Plate

Unsteady viscous flow above an oscillating flat plate was computed using the third-order ENO scheme. The initially steady semi-infinite fluid was set into motion when the solid plate at $y = 0$ began to oscillate with velocity given by

$$u_{\text{plate}} = u_0 \sin \omega t \tag{10}$$

The exact solution of this problem can be found in Ref. 17.

The two-dimensional Navier–Stokes equations were solved using the third-order ENO scheme. Flow conditions were the same as those used in Rogers and Kwak.[18] The dimensionless frequency was unity, and $u_0 = 40$ m/s. Periodic boundary condition was used in x direction. The density, pressure, and temperature were assumed to be constant both at the wall and in the far field.

Figure 4 shows the velocity distribution at the end of eight periods of computations. The numerical results were obtained using 20 grid points between $Y = 0$–6. The CFL number based on the inviscid terms was 0.5. The figure shows that the numerical solution agrees well with the exact solution.

The results of these test cases indicate that ENO schemes of high-order accuracy perform well in simulating transient viscous flows.

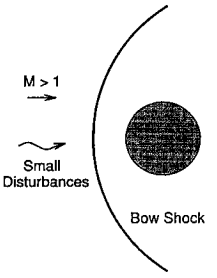

Fig. 5 Schematic of shock–disturbance interaction for hypersonic flow over a cylinder.

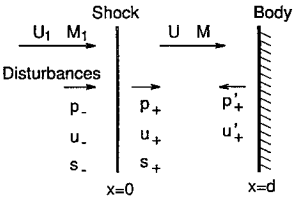

Fig. 6 One-dimensional model used by Morkovin[4] for bow-shock–disturbance interaction.

Bow-Shock–Acoustic-Wave Interactions

Linear Analysis

Figure 5 shows a schematic of the bow-shock–disturbance interactions in hypersonic flow past a cylinder. When the bow shock is perturbed from its steady configuration by a disturbance wave from the freestream, the interaction generates three types of waves[19] behind the shock:

1) Acoustic waves, which propagate with the speed of sound relative to the moving fluid, $\delta p \neq 0$, $\delta\rho = (\delta p/c^2)$, $\delta u = (\delta p/\rho c)$, and $\delta s = \delta W = 0$.

2) Entropy waves, which convect with the moving fluid, $\delta s \neq 0$, $\delta\rho = (\partial\rho/\partial S)_p\, \delta s$, and $\delta u = \delta p = \delta W = 0$.

3) Vorticity waves, which also convect with the moving fluid, $\delta W \neq 0$, $\delta u \neq 0$, and $\delta\rho = \delta p = \delta s = 0$.

These three types of disturbance waves propagate downstream independently, connected only through the boundary conditions at the shock wave and at the wall. The acoustic waves, which travel along Mach lines, reach the wall and reflect back to the shock upstream. These reflections and interactions of the acoustic waves change the wave structure behind the bow shock considerably. On the other hand, the vorticity and entropy waves propagate along streamlines and do not reflect on the wall surface.

Following the method of Morkovin,[4] the bow-shock–acoustic-wave interaction along the stagnation line can be formulated approximately as a one-dimensional problem (Fig. 6). The mean flow variables between the shock wave and the body are assumed to be uniform. The disturbance pressure, density, and entropy on the upstream (denoted by subscript $-$) and downstream (denoted by subscript $+$) sides of the shock wave are nondimensionalized by their respective local mean variables as follows:

$$p_\pm = \delta p/\gamma p, \qquad u_\pm = \delta u/c, \qquad s_\pm = \delta S/c_p \tag{11}$$

The upstream disturbances are assumed to be a planar disturbance wave with a single frequency, i.e.,

$$p_- = A_{p_-} \exp\left\{i\omega\left[t - \frac{x}{c_1(1+M_1)}\right]\right\}$$
$$u_- = A_{u_-} \exp\left\{i\omega\left[t - \frac{x}{c_1(1+M_1)}\right]\right\} \tag{12}$$
$$s_- = A_{s_-} \exp\{i\omega[t - (x/c_1M_1)]\}$$

where $A_{s_-} = 0$ if there is only an acoustic wave in the freestream, and $A_{p_-} = A_{u_-} = 0$ if there is only an entropy wave in the freestream. The waves behind the bow shock are the combination of downstream-propagating waves (acoustic and entropy waves) and upstream-propagating acoustic wave reflected from the wall, i.e.,

$$p_+ = A_{p_+} \exp\left\{il + i\omega\left[t - \frac{x}{c(1+M)}\right]\right\} + A_{p'_+} \exp\left\{in + i\omega\left[t + \frac{x}{c(1-M)}\right]\right\}$$
$$u_+ = A_{u_+} \exp\left\{il + i\omega\left[t - \frac{x}{c(1+M)}\right]\right\} + A_{u'_+} \exp\left\{in + i\omega\left[t + \frac{x}{c(1-M)}\right]\right\} \tag{13}$$
$$s_+ = A_{s_+} \exp\{im + i\omega[t - (x/cM)]\}$$

The perturbed-bow-shock shape is

$$\psi = -iA_\psi \exp(ij + i\omega t) \tag{14}$$

where j, l, m, and n are the phase angles.

If magnitudes of the disturbances are small, the Rankine–Hugoniot relations for a perturbed normal shock wave can be linearized as:

$$\begin{bmatrix} s_+ \\ p_+ \\ u_+ \end{bmatrix} - \begin{bmatrix} \Pi_{11} \\ \Pi_{21} \\ \Pi_{31} \end{bmatrix} \frac{1}{c}\frac{\partial \psi}{\partial t} = \begin{bmatrix} \Lambda_{11} & \Lambda_{12} & \Lambda_{13} \\ \Lambda_{21} & \Lambda_{22} & \Lambda_{23} \\ \Lambda_{31} & \Lambda_{32} & \Lambda_{33} \end{bmatrix} \begin{bmatrix} s_- \\ p_- \\ u_- \end{bmatrix} \tag{15}$$

where the coefficients, such as Λ_{11} and Π_{11}, can be found in Ref. 4. The velocity boundary condition on the wall leads to

$$A'_{u_+} = -A_{u_+}, \qquad l = n + \frac{2\omega d}{c(1-M^2)} + 2N\pi \tag{16}$$

where N is an arbitrary integer. From acoustic theory, the amplitudes of downstream- and upstream-moving acoustic waves satisfy

$$A_{p_+} = A_{u_+}, \qquad A_{p'_+} = -A_{u'_+} \tag{17}$$

From Eqs. (15–17), we can solve the wave parameters behind the shock, s_+, p_+, and u_+, as functions of mean flow parameters and the freestream wave parameters. For the present case of freestream acoustic-wave interaction, the solution of the pressure disturbance behind the shock wave can be obtained as

$$\frac{p_+}{A_{u_-}} \exp\left\{-i\omega\left[t + \frac{x}{c(1-M)}\right]\right\} = \frac{\Omega_{23}}{P_{23}\exp[(2i\omega d)/c(1-M^2)] - P_{23}^+} \times \left\{1 + \exp\left[\frac{2i\omega(d-x)}{c(1-M^2)}\right]\right\} \tag{18}$$

where

$$P_{23}^+ = \Pi_{21} + \Pi_{31} \qquad P_{23} = \Pi_{21} - \Pi_{31}$$
$$\Omega_{23} = \Pi_{21}(\Lambda_{32} + \Lambda_{33}) - \Pi_{31}(\Lambda_{22} + \Lambda_{23}) \tag{19}$$

Taking the absolute values of both sides of Eq. (18) leads to the amplitudes of pressure and velocity perturbations downstream of the shock along the stagnation line. In particular, it can be shown that the magnitude of pressure perturbation on the body surface is

$$\left|\frac{p_+(d)}{A_{u_-}}\right| = \frac{|2\Omega_{23}|}{\left\{P_{23}^2 + P_{23}^{+2} - 2P_{23}P_{23}^+ \cos[(2\omega d)/c(1-M^2)]\right\}^{\frac{1}{2}}} \tag{20}$$

and it is always greater than the magnitudes away from the body.

On the other hand, at the initial moment of introducing the disturbance wave in the freestream, the induced disturbance waves behind the bow shock contain only downstream-moving waves. Under such a condition, the linearized solution of the disturbance waves behind the shock can be found in Ref. 20 as

$$\left|\frac{p_+}{p_-}\right| = \frac{p}{p_1}\frac{2M_1^4 + 2(\gamma+1)M_1^3 + (3\gamma-1)M_1^2 - \gamma + 1}{(\gamma+1)\left(1 + M_1^2 + 2MM_1^2\right)} \tag{21}$$

This equation also can be derived from Eq. (15) and it is valid at the initial moment of imposing freestream waves until the acoustic waves reflected from the wall reach back to the bow shock.

Numerical Simulation

The bow-shock–freestream acoustic-wave interaction in hypersonic flow past a cylinder was computed using the ENO schemes to solve the Euler equations. The freestream Mach number was 8.03, and the cylinder radius was 0.0381 m. The calculations were carried out in two steps: 1) computing a steady flowfield, and 2) computing the bow-shock–acoustic wave interaction problem by imposing an acoustic disturbance wave to the freestream boundary. The numerical solutions along the stagnation line were compared with the results of linear Morkovin analysis. The time history of the pressure fluctuations behind the bow shock was compared with the linear analytical results by McKenzie and Westphal.[20] Meanwhile, grid refinement studies were carried out to check the accuracy of the numerical solutions.

Steady-Flowfield Solutions

Since it is difficult to obtain steady-state solutions using high-order ENO schemes, a second-order ENO scheme was used to obtain steady-flow solutions. Figure 7 shows the steady-pressure and density distributions along the stagnation line using two sets of coarse (100×80) and fine (200×160) grids. The steady-pressure contours from coarse-grid computations are shown in Fig. 8. The results show that the mean flowfield was well resolved with these grids.

Even with the second-order ENO schemes, slight oscillations in the steady-flow solutions were observed. Figures 9 and 10 show the

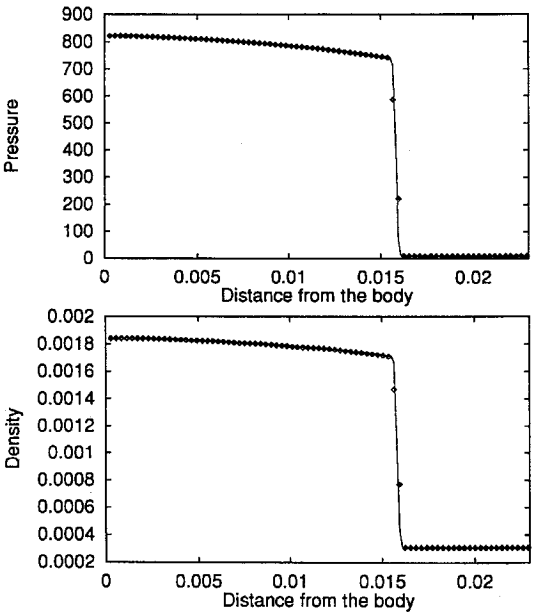

Fig. 7 Distribution of mean pressure and density along the stagnation line (M = 8.03): ♦, coarse grid and —, fine grid.

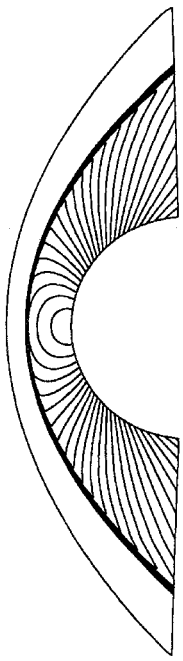

Fig. 8 Pressure contours of mean flow calculation using coarse grids (100 × 80).

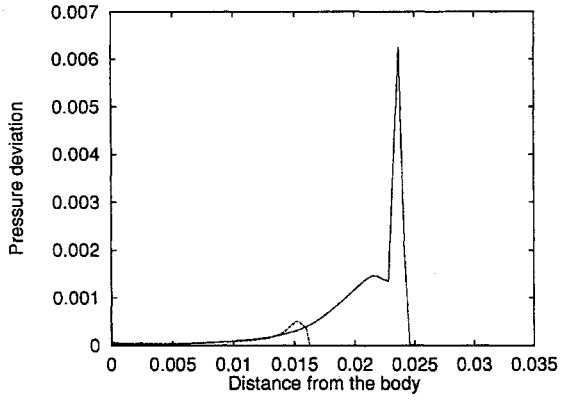

Fig. 9 Root-mean-square distribution of pressure oscillations along θ = 48.6-deg (—) and 0-deg (- - -) lines.

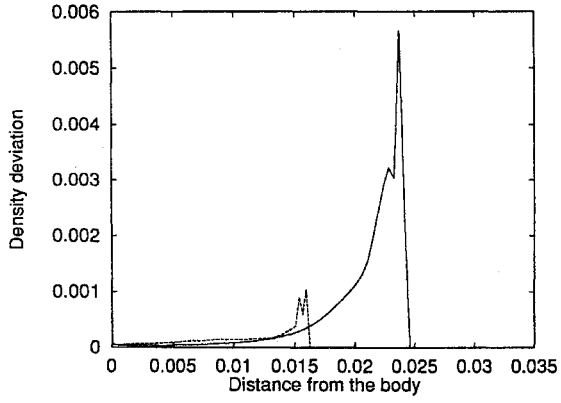

Fig. 10 Root-mean-square distribution of density oscillations along θ = 48.6-deg (—) and 0-deg (- - -) lines.

distributions of the root-mean-square (rms) values of dimensionless pressure and density fluctuations along two grid lines (θ = 0, 48.6 deg). The figures show that the oscillations of steady-flow solutions are mainly located near the bow shock, and the magnitudes of the oscillations are very small in the flowfield. These numerical oscillations can be damped out by using the TVD schemes with stronger numerical dissipation. However, since the levels of oscillations of the steady solutions are small compared with the magnitude of physical disturbances introduced in the unsteady calculations, the steady-state solutions of the second-order ENO schemes are acceptable.

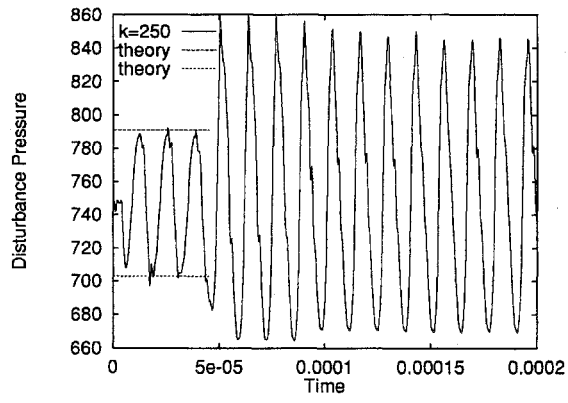

Fig. 11 Time history of instantaneous pressure behind the shock (M = 8.03, k = 250 m^{-1}).

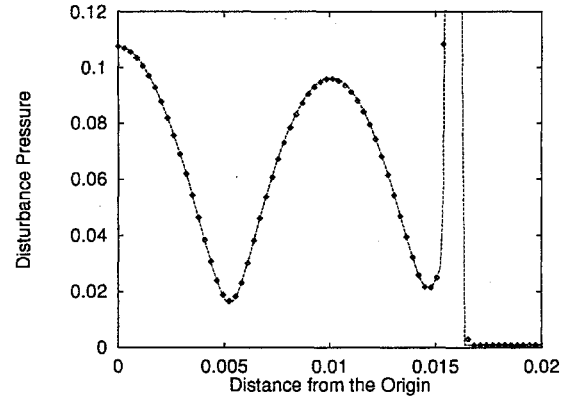

Fig. 12 Grid refinement study for rms disturbance pressure calculation (k = 125 m^{-1}): ♦, coarse grid and - - -, fine grid.

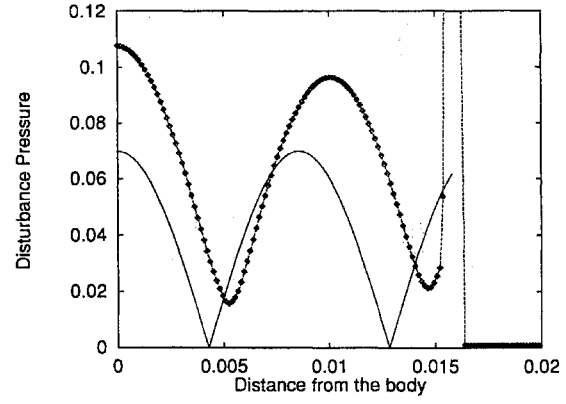

Fig. 13 Distribution of rms disturbance pressure along the stagnation line (k = 125 m^{-1}): —, Morkovin and ♦, numerical.

Bow-Shock–Acoustic-Wave Interaction

Having obtained the steady flowfield, we introduced the following acoustic disturbances to the steady solutions at the freestream boundary:

$$\delta q = \Delta q \exp\{ik[x - (u + c)t]\} \tag{22}$$

where q can be u, v, p, or ρ, and

$$\Delta u = \epsilon_0 u_\infty, \qquad \Delta v = 0 \qquad \Delta p = \rho_\infty c_\infty \Delta u$$
$$\Delta \rho = \Delta p / c_\infty^2 \qquad \epsilon_0 = 0.01 \tag{23}$$

In the computations, three wave numbers—k = 125, 170, 250 m^{-1}—and a CFL number of approximately 0.8 were used. All the unsteady computations were performed for 30 disturbance periods. Afterward, the rms values of the disturbance-flow quantities were calculated for about 25 periods. The rms values of the disturbance variables were the numerical solutions of the spatial distribution of the magnitudes of the disturbance waves.

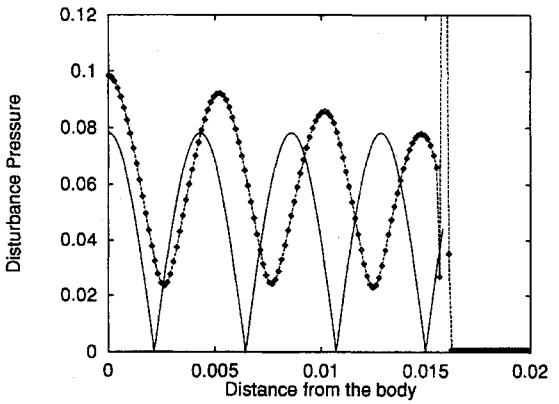

Fig. 14 Distribution of rms disturbance pressure along the stagnation line ($k = 250\ \mathrm{m}^{-1}$): —, Morkovin and ♦, numerical.

Figure 11 shows the time history of disturbance pressure at a fixed point immediately behind the bow shock along the stagnation line for the case of wave number $k = 250\ \mathrm{m}^{-1}$. Two discrete zones can be observed in Fig. 11. The first zone only contains downstream-moving acoustic waves at the initial moments of introducing the freestream wave. The second zone contains both the downstream- and upstream-moving acoustic waves after the reflected acoustic waves reach back to the shock. The straight lines in the first zone are the theoretical maximum and minimum values given by Eq. (21). Because no disturbances can transmit through the shock and propagate upstream, these acoustic waves are reflected back and forth in the region between the shock and the body. Because the reflection coefficient[20] of acoustic waves incident behind the normal shock cannot exceed unity for perfect gas, the resonance of acoustic waves cannot build up, and the bow shock in a perfect gas is always stable.

Figure 12 shows the results of rms disturbance pressure distribution along the stagnation line from both coarse- and fine-grid

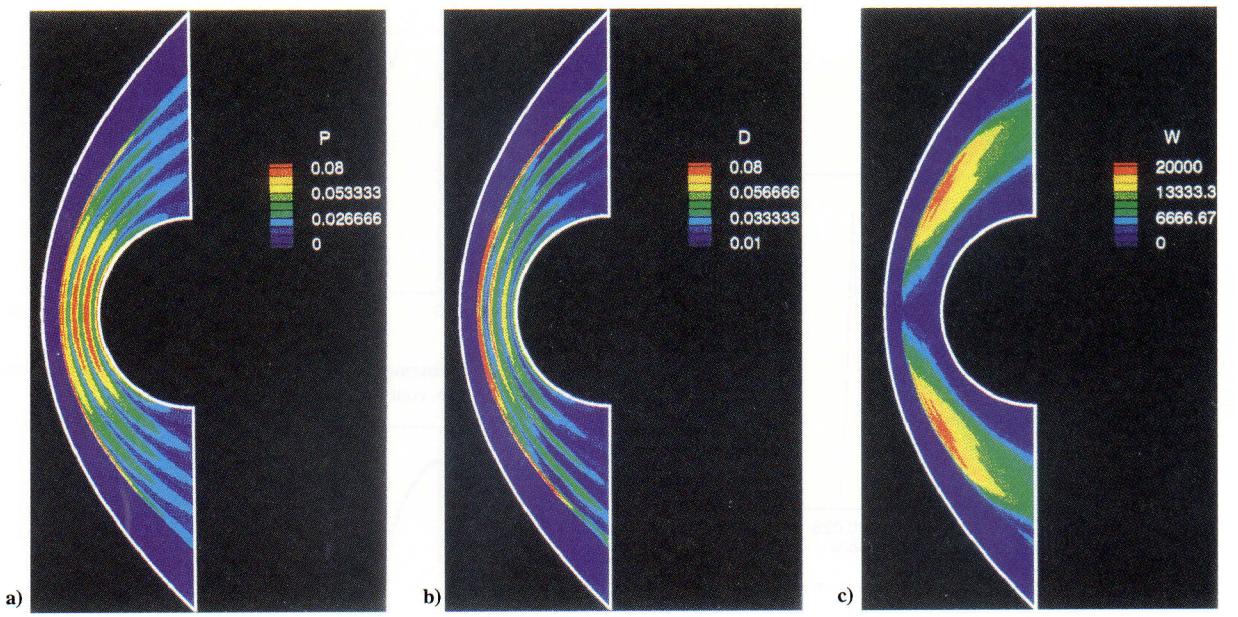

Fig. 15 Contours of rms disturbance: a) pressure, b) density, and c) vorticity ($k = 250\ \mathrm{m}^{-1}$).

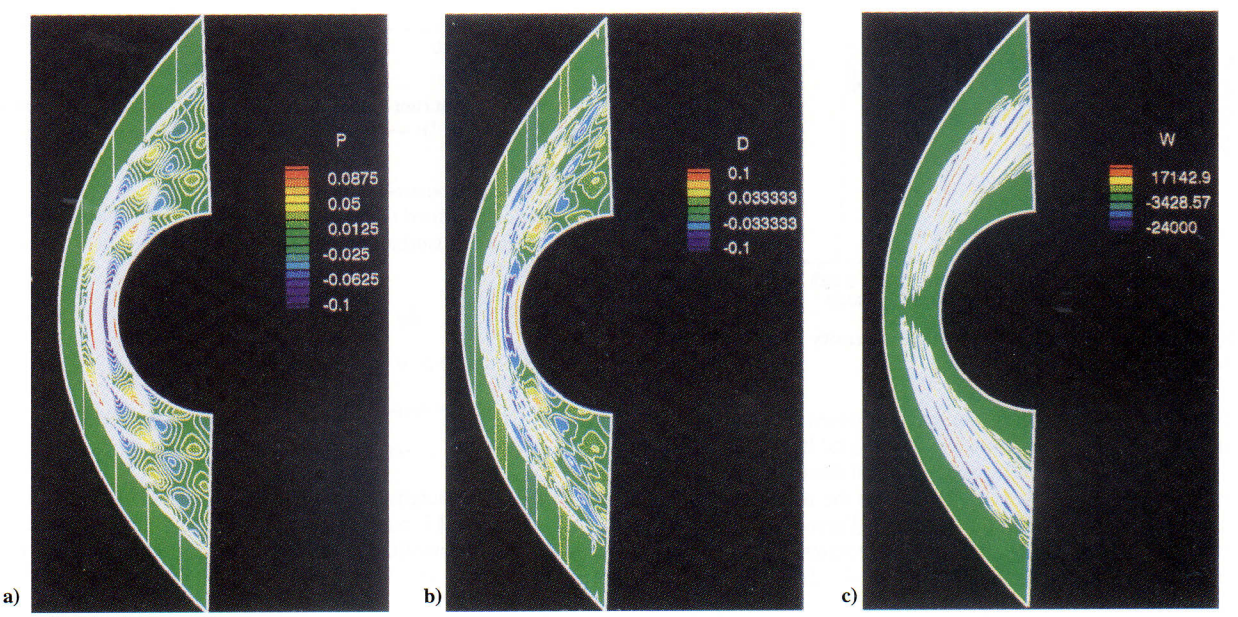

Fig. 16 Contours of instantaneous disturbance: a) pressure, b) density, and c) vorticity ($k = 250\ \mathrm{m}^{-1}$).

computations with wave number $k = 125\ \mathrm{m}^{-1}$. The results show that current grids are accurate enough to resolve the transient acoustic flow features.

Figures 13 and 14 show the comparison of numerical solutions with analytical ones for the magnitudes of pressure waves at different freestream frequencies. The solid lines correspond to the analytical values obtained from Eq. (20). The wavelengths from numerical calculations are slightly larger than those from analytical solutions. Numerical amplitudes of the pressure waves are also greater than those predicted by the linear analysis. This discrepancy is caused by the simplified assumption of uniform steady flowfield behind the shock used in the analytical analysis. In reality, the steady flow downstream from the shock is not uniform. The difference in wavelength can be verified easily as follows. From Eq. (20), the wavelength λ in the rms value of the pressure waves is

$$\frac{2\omega\lambda}{c(1-M^2)} = 2\pi \tag{24}$$

Substituting $\omega = k(u_1 + c_1)$ for freestream acoustic waves results in

$$\lambda = \frac{\pi c(1-M^2)}{kc_1(1+M_1)} \tag{25}$$

Since the mean flow velocity as well as M is decelerating toward the wall, the wavelength given by the above equation will become larger than that obtained from uniform flow assumption. This also will affect the amplitudes of disturbances. Therefore, there is the additional amplification of disturbance properties in the numerical solutions near the wall, as shown in Figs. 13 and 14.

Figure 15 shows the contours of rms disturbance pressure, density, and vorticity with $k = 250\ \mathrm{m}^{-1}$. The results show that the maximum disturbance pressure is located at the stagnation point. Amplitudes of disturbances drop an order of magnitude as these disturbances propagate away from the stagnation line. Other numerical results using a different freestream Mach number show a similar trend.

Figure 16 shows the contours of instantaneous disturbance pressure, density, and vorticity. The amplified acoustic wave pattern can be observed in Fig. 16a. Since the disturbance density field is composed of both acoustic and entropy waves with the following dimensionless relation:

$$\delta\rho = \delta p + \delta s \tag{26}$$

the flow pattern of the instantaneous density field is more complex than that of the disturbance pressure field shown in Fig. 16a. However, two zones downstream of the shock can be roughly seen. The first zone, which is near the shock, is composed of both acoustic and entropy waves. The second one, which is near the body, is composed mainly of acoustic waves.

The results also show that uniform freestream acoustic waves become very nonuniform in magnitude after they interact with the bow shock and with the reflected waves from the cylinder. The disturbances magnitudes are amplified greatly by the reflection near the stagnation region. These results can be valuable to the understanding of the effect of shock–disturbances interactions on the receptivity and transition of hypersonic boundary layers.

Conclusions

ENO schemes of high-order accuracy have been applied to the two-dimensional Euler and Navier–Stokes equations for studying transient hypersonic viscous flows. The grid refinement studies on the linear convection–diffusion equation show that the ENO schemes maintain their theoretical orders of accuracy in these test cases. Numerical analyses of Stokes oscillating plate indicate that the high-order ENO schemes are suitable for calculating unsteady flows with solid boundaries.

The interactions of freestream acoustic waves with a strong bow shock wave in hypersonic flow past a cylinder have been studied using the third-order ENO scheme. Numerical results along the stagnation line agree reasonably well with the linear analytical solutions; the differences between the two solutions are caused by the simplified assumption used in the linear analysis that the mean flow behind the shock is uniform. The results show that the disturbances downstream of the shock are considerably amplified by the wave interactions and reflections between the shock and the wall. The disturbance waves become very nonuniform in magnitude near the cylinder, and the maximum pressure wave magnitude is always located at the stagnation point. These results show that the bow shock wave has strong effects on the receptivity of hypersonic boundary layers.

Acknowledgments

This research was supported by U.S. Air Force Office of Scientific Research Grants F49620-92-J-0090 and F49620-94-1-0019 monitored by Leonidas Sakell.

References

[1]Committee on Hypersonic Technology for Military Application, National Research Council, *Hypersonic Technology for Military Application*, National Academy Press, Washington, DC, 1989.

[2]Reshotko, E., "Hypersonic Stability and Transition," *Hypersonic Flows for Reentry Problems*, edited by J.-A. Desideri, R. Glowinski, and J. Periaux, Vol. 1, Springer–Verlag, Berlin, 1991, pp. 18–34.

[3]Zhong, X., "Application of High-Order ENO Schemes to Unsteady Hypersonic Shock–Shock Interference Heating on a Cylinder," *AIAA Journal*, Vol. 32, No. 8, 1994, pp. 1606–1616.

[4]Morkovin, M. V., "Note on the Assessment of Flow Disturbances at a Blunt Body Traveling at Supersonic Speeds Owing to Flow Disturbances in Free Stream," *Journal of Applied Mechanics*, Vol. 27, No. 6, 1960, pp. 223–229.

[5]Choudhari, M., and Streett, C., "Boundary Layer Receptivity Phenomena in Three-Dimensional and High-Speed Boundary Layers," AIAA Paper 90-5258, Oct. 1990.

[6]Harten, A., Engquist, B., Osher, S., and Chakravarthy, S., "Uniformly High Order Accurate Essentially Non-Oscillatory Schemes, III," *Journal of Computational Physics*, Vol. 71, 1987, pp. 231–303.

[7]Rogerson, A. M., and Meiburg, E., "A Numerical Study of the Convergence Properties of ENO Schemes," *Journal of Scientific Computing*, Vol. 5, No. 2, 1990, pp. 151–167.

[8]Shu, C., "Numerical Experiments on the Accuracy of ENO and Modified ENO Schemes," *Journal of Scientific Computing*, Vol. 5, No. 2, 1990, pp. 127–149.

[9]Liu, X.-D., Osher, S., and Chan, T., "Weighted Essentially Non-Oscillatory Schemes," *Journal of Computational Physics*, Vol. 115, 1994, pp. 200–212.

[10]Shu, C., and Osher, S., "Efficient Implementation of Essentially Non-Oscillatory Shock-Capturing Schemes," *Journal of Computational Physics*, Vol. 77, 1988, pp. 439–471.

[11]Shu, C., and Osher, S., "Efficient Implementation of Essentially Non-Oscillatory Shock-Capturing Schemes, II," *Journal of Computational Physics*, Vol. 83, 1989, pp. 32–78.

[12]Casper, J., "Essentially Non-Oscillatory Shock-Capturing Schemes to Multi-Dimensional Systems of Conservation Laws," Ph.D. Thesis, Old Dominion Univ., Norfolk, VA, Dec. 1990.

[13]Shu, C., Erlebacher, G., Zhang, T. A., Whitaker, D., and Osher, S., "High-Order ENO Schemes Applied to Two- and Three-Dimensional Compressible Flow," CAM Rept. 91-09, Dept. of Mathematics, Univ. of California, Los Angeles, CA, 1991.

[14]Atkins, H. L., "High-Order ENO Methods for the Unsteady Compressible Navier–Stokes Equations," AIAA Paper 91-1557, June 1991.

[15]Casper, J., and Atkins, H. L., "A Finite-Volume High-Order ENO Scheme for Two-Dimensional Hyperbolic Systems," *Journal of Computational Physics*, Vol. 106, 1993, pp. 62–76.

[16]Chiu, C., and Zhong, X., "Simulation of Transient Hypersonic Flow Using the ENO Schemes," AIAA Paper 95-0469, Jan. 1995.

[17]Panton, R. L., *Incompressible Flow*, Wiley, New York, 1984.

[18]Rogers, S. E., and Kwak, D., "Upwind Differencing Scheme for the Time-Accurate Incompressible Navier–Stokes Equation," *AIAA Journal*, Vol. 28, No. 2, 1990, pp. 253–262.

[19]Kovasznay, L. S. G., "Turbulence in Supersonic Flow," *Journal of the Aeronautical Sciences*, Vol. 20, No. 10, 1953, pp. 657–682.

[20]McKenzie, J. F., and Westphal, K. O., "Interaction of Linear Waves with Oblique Shock Waves," *Physics of Fluids*, Vol. 11, No. 11, 1968, pp 2350–2362.